1

Transitions in Fluid Flows

Order in the chaos:
the emergence of fluid flow patterns

One of the most fascinating phenomena in fluid dynamics is that flows can spontaneously reorganize their macro-scale behaviour when external conditions are changed. Such transitions are at the heart of pattern formation in fluids as intensively studied since the early twentieth century. The overall problem is the determination of the different (statistical) equilibrium flow patterns versus the applied forcing and external geometry of the flow. The complicating factor here is that, due to the non-linearity of the underlying processes, multiple flow patterns can exist under the same external conditions.

The study of transition phenomena in flows of liquids and gases is fundamental to many engineering processes, in particular those associated with mass and heat transfer, and hence of great practical interest. Transitions can lead to different momentum regimes (e.g., drag, torque) and heat transfer regimes. These transitions can suddenly (compared to changes in the forcing) lead to different operating conditions. Isothermal flows may undergo qualitative changes in separation behaviour and turbulence intensity; mean flows in turbulent buoyancy-driven convection can change their overall pattern; and plasma flows in a Tokamak reactor suddenly show strong oscillatory behaviour (Crawford and Knobloch, 1991; Dijkstra *et al.*, 2014).

Transitions in environmental flows, for example in weather and climate, are at the moment much studied in connection with climate change. For example, a reorganization of the large-scale Atlantic Ocean circulation may lead to a substantial change in the meridional heat transport affecting land temperatures over a large part of the globe (Rahmstorf, 2000). Critical conditions in such flows, at which they may undergo a large qualitative change, are associated with what is now often referred to as a 'tipping' point (Gladwell, 2000). Sub-components of the climate system with potential transition behaviour are indicated by 'tipping elements'

1

(Lenton *et al.*, 2008). From a practical point of view, one would like to determine these critical conditions and understand how to avoid undesirable transitions.

The fluid flow transitions are also interesting from a complex systems science point of view (Thurner *et al.*, 2018). Due to variations in forcing of the flow, the micro-scale fluid particles organize in particular ways so as to give different macroscopic patterns and hence are an example of emerging behaviour. Subsequent transitions when the forcing of the flow is increased lead to more complicated behaviour and eventually to turbulent flows. Understanding the (staged) transition to turbulence is one of the central problems of classical physics which is, despite much progress over the last decades, still unsolved (Eckert, 2019).

In this first chapter, we will describe canonical fluid dynamical systems which have been used to study flow transitions. The attractive aspects of these flows is that they are easily accessible experimentally and that there are mathematical equations accurately describing their behaviour. After presenting those equations in general form in Section 1.1, the following sections will deal with four typical flow configurations: the Lid-Driven Cavity flow (Section 1.2), the Taylor–Couette flow (Section 1.3), the Rayleigh–Bénard–Marangoni flow (Section 1.4), and the Differentially Heated Cavity flow (Section 1.5). For each case, we will shortly describe typical experimental results and present the specific mathematical equations describing the canonical experimental configuration.

1.1 General Fluid Dynamics Equations

The main set of equations in fluid dynamics describes the conservation of mass, momentum, and thermal energy, and contains an equation of state relating density, pressure, and temperature. We will consider here the case of a Newtonian fluid with constant heat capacity C_p, dynamic viscosity μ, and thermal conductivity k, which is relevant to understanding the results in many experiments.

Conservation of mass is expressed by the continuity equation,

$$\frac{\partial \rho}{\partial t} = \nabla \cdot (\rho \mathbf{u}), \tag{1.1}$$

where ρ is density and $\mathbf{u}$ the velocity vector. The Navier–Stokes equations describe the conservation of momentum. They are written as

$$\rho \left(\frac{\partial \mathbf{u}}{\partial t} + \mathbf{u} \cdot \nabla \mathbf{u} \right) = -\nabla p + \mu \nabla^2 \mathbf{u} + \frac{1}{3} \mu \nabla (\nabla \cdot \mathbf{u}) + \mathbf{f}, \tag{1.2}$$

where p is the pressure and $\mathbf{f}$ represents a body force. One has to interpret the maths shown in Equation (1.2) component-wise.

Thermal energy conservation is expressed as an equation for the temperature T given by

$$\rho C_p \left(\frac{\partial T}{\partial t} + \mathbf{u} \cdot \nabla T \right) = k\nabla^2 T + Q_T, \tag{1.3}$$

where Q_T is a heat source or heat sink.

These equations are supplemented by a general equation of state,

$$\rho = \rho(p, T);$$

for example, the ideal-gas law $p = \rho RT$, where R is the universal gas constant. This leads to six equations for the six unknowns: three components of the velocity, the temperature, the density, and the pressure. In addition to these main equations, there may be equations for so-called tracers, for example chemical components (e.g., salinity in the ocean) and moisture (e.g., in the atmosphere). These additional equations usually have the same form as Equation (1.3), that is, they are of the convection–diffusion type. Also, electromagnetic forces may be involved, for example for studying plasma flows, leading to the addition of Maxwell's equations. All equations have to be supplied with appropriate boundary conditions and an initial condition.

1.2 Lid-Driven Cavity Flow

Due to its simple geometry, the incompressible flow in lid-driven cavities plays an important role in fundamental fluid mechanics and serves often as a numerical benchmark problem. Batchelor (1956) already pointed out that lid-driven cavity flows exhibit almost all the phenomena that can possibly occur in incompressible flows: eddies, secondary flows, complex flow patterns, chaotic particle motions, and turbulence.

1.2.1 Experimental Results

A typical experimental configuration, used by, for example, Koseff and Street (1984), is shown in Fig. 1.1a. The liquid is contained in a three-dimensional cavity characterized by two aspect ratios: that of the length L to depth D, $A_x = L/D$; and that of the width B to depth, $A_y = B/D$. The density of the liquid is constant ρ, its constant kinematic viscosity is $\nu = \mu/\rho$, and the liquid is sheared at its top by a constant velocity U. To realize this, a belt-drive support structure was used in Koseff and Street (1984) in which the belt speed was constant up to 0.5 per cent.

A typical flow observed along the symmetry plane of the cavity (e.g., for $A_x = 1$ and $A_y = 3$ and for a Reynolds number $Re = UL/\nu = 3{,}300$ in Koseff and Street (1984)) is sketched in Fig. 1.1b. Overall, a one-cell flow structure is seen, with surface flow into the direction of the surface velocity, and smaller vortices appear in the corner regions at the bottom. The flow may not be stationary; for example,
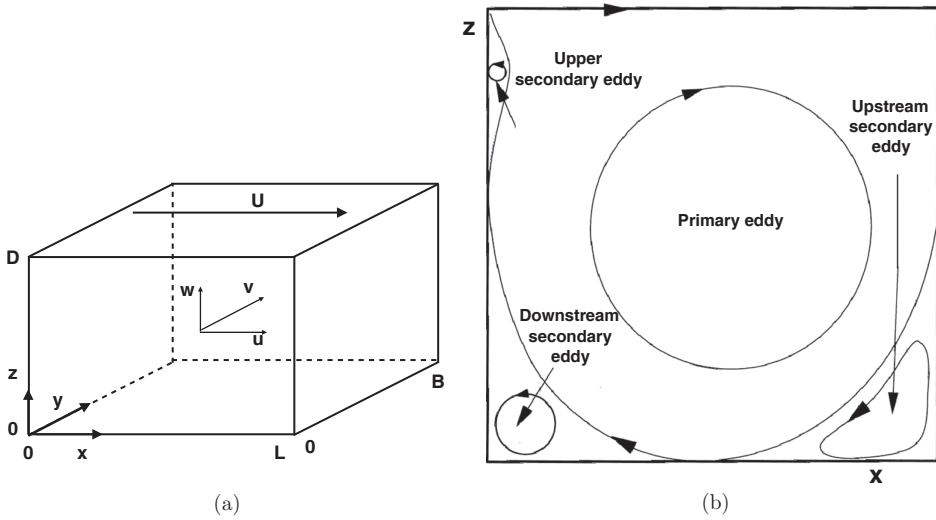
Figure 1.1 (a) Geometry of the lid-driven cavity flow of dimensions, L, B, and D, with a moving lid in the x-direction on the top having velocity U. (b) Typical flow observed in the lid-driven cavity (based on the results of Koseff and Street (1984)).

fluctuations in the vertical velocity were measured for $Re = 3,300$ (Koseff and Street, 1984), with a dominant frequency of about 0.01 Hz. In the streamwise (y-)direction, so-called Taylor–Görtler vortices were found and about eight pairs of vortices were found for $A_y = 3$. An example of this flow structure can be found in Freitas and colleagues (1985) and in Fig. 12 of Kuhlmann and Romanò (2019). The structure of the Taylor–Görtler vortices and the secondary corner vortices depend strongly on the geometry of the container.

For this same configuration ($A_x = 1, A_y = 3$), Aidun and colleagues (1991) found a stationary flow for values of Re up to $Re_c = 875 \pm 50$ and oscillatory flow for higher values of Re, in agreement with the results in Koseff and Street (1984) for $Re = 3,300$. For very large values of Re (e.g., Koseff and Street (1984) use $Re = 10,000$), irregular (turbulent) flows are found. An experimental regime diagram, mapping out the value of Re_c versus the parameters A_x and A_y and showing secondary flow types for higher values of Re, does not appear to be available in the literature.

This short summary of the experimental result on the lid-driven cavity flow already leads to intriguing fluid dynamical questions. For example, why is there a critical value of Re marking the transition from steady to oscillatory flows? Many other issues, for example the spatial structure of the corner flows and the dependence of the Taylor–Görtler vortices on A_y, have led to a number of fundamental theoretical studies (Kuhlmann and Romanò, 2019).

1.2.2 Governing Equations

Following the experimental setup used in Koseff and Street (1984), we consider the flow of a constant density Newtonian fluid in a three-dimensional cavity with length L, width B, and height D (Fig. 1.1a). The fluid motion has velocity vector $\mathbf{u} = (u, v, w)^T$ and is driven by a moving lid on the top with constant velocity U into the positive x-direction.

The governing equations for this problem are the incompressible Navier–Stokes equations given by

$$\frac{\partial u}{\partial t} + u\frac{\partial u}{\partial x} + v\frac{\partial u}{\partial y} + w\frac{\partial u}{\partial z} \;=\; -\frac{1}{\rho}\frac{\partial p}{\partial x} + \nu\nabla^2 u + f_x, \tag{1.4a}$$

$$\frac{\partial v}{\partial t} + u\frac{\partial v}{\partial x} + v\frac{\partial v}{\partial y} + w\frac{\partial v}{\partial z} \;=\; -\frac{1}{\rho}\frac{\partial p}{\partial y} + \nu\nabla^2 v + f_y, \tag{1.4b}$$

$$\frac{\partial w}{\partial t} + u\frac{\partial w}{\partial x} + v\frac{\partial w}{\partial y} + w\frac{\partial w}{\partial z} \;=\; -\frac{1}{\rho}\frac{\partial p}{\partial z} + \nu\nabla^2 w + f_z, \tag{1.4c}$$

$$\frac{\partial u}{\partial x} + \frac{\partial v}{\partial y} + \frac{\partial w}{\partial z} \;=\; 0, \tag{1.4d}$$

with $f_x = f_y = 0$ and $f_z = -g$, where g is the gravitational acceleration. *See example Ex. 1.1*

The boundary conditions are given by no-slip conditions on all the walls, formulated as

$$x = 0, L: \quad u = v = w = 0, \tag{1.5a}$$

$$y = 0, B: \quad u = v = w = 0, \tag{1.5b}$$

$$z = 0: \quad u = v = w = 0, \tag{1.5c}$$

$$z = D: \quad u = U, v = w = 0. \tag{1.5d}$$

As we will see in Chapter 10, for a given geometry and boundary conditions, the Reynolds number $Re = UL/\nu$ is determining the flow completely. There is no elementary non-trivial analytical solution known for the Lid-Driven Cavity flow.

Additional Material

- A relatively recent and extensive review of experimental results on the Lid-Driven Cavity flow can be found in Kuhlmann and Romanò (2019). They discuss also experimental results for extended configurations, for example where two walls of the cavity move with a (different) constant velocity.
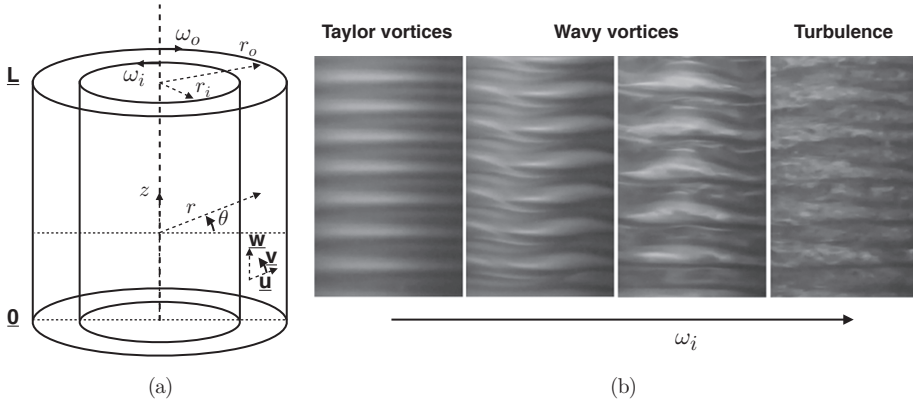
Figure 1.2 (a) Sketch of the Taylor–Couette flow configuration. (b) Observed pattern of Taylor vortices for four different values of the inner rotation rate ω_i, which increases from left to right (source: https://advlabs.aapt.org/wiki/Taylor-Couette_Flow), with $\omega_o = 0$.

1.3 Taylor–Couette Flow

The flow between concentric cylinders, or Taylor–Couette flow, is one of the canonical pattern formation flows, sometimes referred to as the 'Hydrogen Atom' or 'Drosophila' of fluid dynamics. It shows a staged transition to turbulence, for example as the rotation rate of the inner cylinder is increased, with a very rich behaviour.

1.3.1 Experimental Results

A typical experimental configuration (Fig. 1.2a) consists of two rotating cylinders enclosing a fluid. The inner cylinder of radius r_i rotates with angular velocity ω_i, and the outer one (radius r_o) with angular frequency ω_o. The cylinders have a finite length L, hence the geometry is characterized by the aspect ratio $\Gamma = L/d, d = r_o - r_i$, and the radius ratio $\eta = r_i/r_o$. The fluid has a constant density ρ and constant kinematic viscosity ν, and in this way the flow is characterized by the two Reynolds numbers

$$Re_i = \frac{r_i \omega_i d}{\nu} \, , \; Re_o = \frac{r_o \omega_o d}{\nu}. \tag{1.6}$$

The first experiments were carried out by Taylor (1923) for the case $\omega_o = 0$, hence with only the inner cylinder rotating. For small values of ω_i a parallel flow exists, which can be determined analytically (see Subsection 1.3.2). As this flow was already observed experimentally by Couette (1890), it was named the Couette flow. Taylor observed that when ω_i exceeds a critical value, instability sets in

and rows of cellular vortices develop. This is the so-called Taylor vortex flow, of which an example is shown in the 'Taylor vortices' panel of Fig. 1.2b. When ω_i is increased to higher values, the cell rows start to move in a wavy fashion after a transition to time dependence (two middle 'Wavy vortices' panels of Fig. 1.2b). For higher values of ω_i, the Taylor cells break down and a turbulent statistical equilibrium flow is established ('Turbulence' panel of Fig. 1.2b).

A theoretical analysis in the case of $\omega_o = 0$ and $\Gamma \to \infty$ (i.e., infinitely long cylinders) to explain the first transition from the Couette flow to the Taylor vortex flow was already done by Taylor (1923). The critical value of Re_i^c for $\eta = 0.8$ is given by $Re_i^c = 94.7$, and for $\eta = 0.9$ it is $Re_i^c = 131.6$ (Recktenwald *et al.*, 1993). Often, another parameter is used to characterize this critical condition for transition, the Taylor number Ta:

$$Ta = 4Re_i^2 \frac{1-\eta}{1+\eta}, \qquad (1.7)$$

with $Ta_c = 3,986$ for $\eta = 0.8$. The critical values agree well with experiments in very long cylinders (Chandrasekhar, 1961; Drazin and Reid, 2004; Chossat and Iooss, 2012). Snyder (1968) has given a semi-empirical equation for the critical condition from collected experimental data.

Detailed work on the Taylor vortex flows (which appear after the first transition) has been done by Mullin and coworkers (Mullin and Blohm, 2001; Mullin *et al.*, 2017). For $\eta = 0.833$, the regime diagram is given in Fig. 1.3, as based on Andereck and colleagues (1986). The complexity of the different flow regimes is striking, given the simplicity of the geometry and forcing, and there are still some unexplored regimes.

1.3.2 Governing Equations

For the configuration in Fig. 1.2a, the incompressible Navier–Stokes equations are conveniently written in cylindrical coordinates (r, θ, z) and the velocity vector (radial, azimuthal, and axial) as $\mathbf{u} = (u, v, w)^T$. The resulting equations are given by

$$\frac{\partial u}{\partial t} + u\frac{\partial u}{\partial r} + \frac{v}{r}\frac{\partial u}{\partial \theta} + w\frac{\partial u}{\partial z} - \frac{v^2}{r} =$$
$$\nu\left(\frac{1}{r}\frac{\partial}{\partial r}\left(r\frac{\partial u}{\partial r}\right) + \frac{1}{r^2}\frac{\partial^2 u}{\partial \theta^2} - \frac{u}{r^2} - \frac{2}{r^2}\frac{\partial v}{\partial \theta} + \frac{\partial^2 u}{\partial z^2}\right) - \frac{1}{\rho}\frac{\partial p}{\partial r} \quad -f_r, \qquad (1.8a)$$

$$\frac{\partial v}{\partial t} + u\frac{\partial v}{\partial r} + \frac{v}{r}\frac{\partial v}{\partial \theta} + w\frac{\partial v}{\partial z} + \frac{uv}{r} =$$
$$\nu\left(\frac{1}{r}\frac{\partial}{\partial r}\left(r\frac{\partial v}{\partial r}\right) + \frac{1}{r^2}\frac{\partial^2 v}{\partial \theta^2} - \frac{v}{r^2} + \frac{2}{r^2}\frac{\partial u}{\partial \theta} + \frac{\partial^2 v}{\partial z^2}\right) - \frac{1}{\rho}\frac{1}{r}\frac{\partial p}{\partial \theta} \quad -f_\theta, \qquad (1.8b)$$
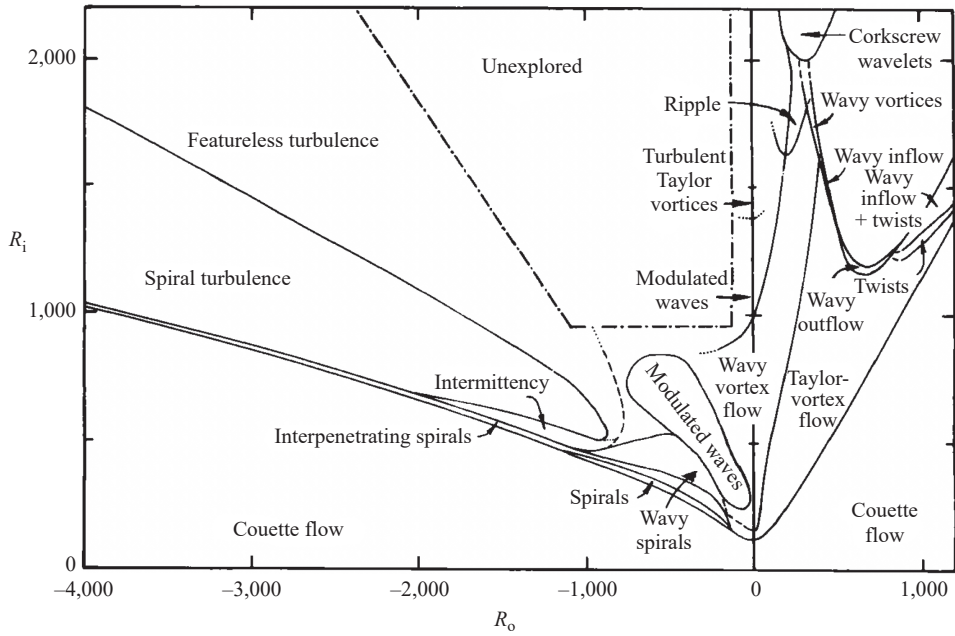
Figure 1.3 Regime diagram for the different flows as observed in Taylor–Couette flow experiments as from Andereck and colleagues (1986) for the case $\eta = 0.833$ and $\Gamma = 30$; here $R = Re$. (Published with permission from Cambridge University Press.)

$$\frac{\partial w}{\partial t} + u\frac{\partial w}{\partial r} + \frac{v}{r}\frac{\partial w}{\partial \theta} + w\frac{\partial w}{\partial z} \quad =$$

$$\nu(\frac{1}{r}\frac{\partial}{\partial r}(r\frac{\partial w}{\partial r}) + \frac{1}{r^2}\frac{\partial^2 w}{\partial \theta^2} + \frac{\partial^2 w}{\partial z^2}) - \frac{1}{\rho}\frac{\partial p}{\partial z} \quad -f_z, \qquad (1.8c)$$

$$\frac{1}{r}\frac{\partial(ru)}{\partial r} + \frac{1}{r}\frac{\partial v}{\partial \theta} + \frac{\partial w}{\partial z} \quad = 0, \qquad (1.8d)$$

with $f_r = f_\theta = 0$ and $f_z = -g$.

The boundary conditions are given by

$$r = r_i: \quad u = w = 0, v = \omega_i r_i, \qquad (1.9a)$$

$$r = r_o: \quad u = w = 0, v = \omega_o r_o, \qquad (1.9b)$$

$$z = 0, L: \quad u = v = w = 0. \qquad (1.9c)$$

Periodic conditions apply in the θ direction, that is, $u(r, 0, z, t) = u(r, 2\pi, z, t)$ with similar conditions for the other velocity components and the pressure.

An analytical solution $(\bar{u}, \bar{v}, \bar{w}, \bar{p})$ of the equations, the Couette flow (Couette, 1890), exists for infinitely long cylinders ($L \to \infty$) and is given by

$$\bar{u} = \bar{w} = 0 \ , \ \bar{v} = ar + \frac{b}{r} \ , \ \bar{p} = -\rho g z + p_d(r), \tag{1.10a}$$

$$a = \frac{\omega_o r_o^2 - \omega_i r_i^2}{r_o^2 - r_i^2} \ , \ b = \frac{(\omega_i - \omega_o) r_o^2 r_i^2}{r_o^2 - r_i^2}, \tag{1.10b}$$

where $p_d(r) = \rho \int_{r_i}^{r} \bar{v}^2 / r \, dr$. There are also analytical solutions (in Bessel function series form) for $\omega_o = 0$ in finite-length containers (Wendl, 1999). *See example Ex. 1.2*

Additional Material

- An extensive review of experimental results on the Taylor–Couette flow can be found in Koschmieder (1993) and Grossmann and colleagues (2016). There is a very accessible Scholarpedia paper on the Taylor–Couette flow by Richard Lueptow, see www.scholarpedia.org/article/Taylor-Couette_flow, where also many other sources (videos, webpages) on the experimental results are provided.
- Since 1979, an international workshop, the ICTW (International Couette–Taylor Workshop), is organized bi-annually; see https://pof.tnw.utwente.nl/ictw/history.html.

1.4 Rayleigh–Bénard–Marangoni Flow

The Rayleigh–Bénard–Marangoni problem is another classic in fluid dynamics. A liquid layer heated from below shows a fascinating and rich set of flow patterns once a critical vertical temperature gradient is exceeded (Koschmieder, 1993).

1.4.1 Experimental Results

First experiments were carried out by Bénard (1901), with a circular container being filled with a viscous liquid such as silicone oil (Fig. 1.4a) with constant heat capacity C_p, dynamic viscosity μ, and thermal conductivity k. Air was situated above the upper surface of the liquid, and the temperature far from the air–liquid interface was nearly constant. This creates a temperature difference, $\Delta T = T_B - T_A$, between the bottom of the container and the surface of the liquid.

When the initially motionless liquid is heated from below, the liquid remains motionless below a critical value of ΔT, say ΔT_c. In this case, the heat transfer through the layer is only by heat conduction. When the temperature difference slightly exceeds ΔT_c, the liquid is set into motion and after a while the flow organizes itself into steady (often hexagonal) cellular patterns (Fig. 1.4b).

For the liquid, a linear equation of state,

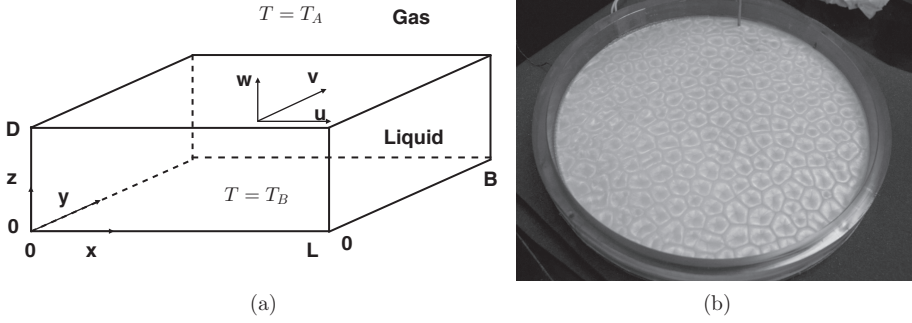$$\rho = \rho_0(1 - \alpha_T(T - T_0)), \tag{1.11}$$

Figure 1.4 (a) Sketch of the model set-up and boundary conditions of the Rayleigh–Bénard–Marangoni problem. (b) Example of a flow pattern consisting of hexagons arising in a liquid heated from below (Matsson, 2008); see https://peer.asee.org/a-student-project-on-rayleigh-benard-convection.

is usually an adequate approximation, where α_T is the thermal compressibility coefficient, T_0 a reference temperature, and ρ_0 a reference density. In situations with an air–liquid interface, such as in Fig. 1.4a, the surface tension σ depends on the temperature. For many liquids, including water, a relation of the form

$$\sigma = \sigma_0(1 - \gamma_T(T - T_0)) \tag{1.12}$$

holds, where σ_0 is a reference surface tension. In this case, the surface tension decreases with increasing temperature, and γ_T is a constant. Surface tension gradients give rise to shear stresses (this is the Marangoni effect), with flows directed from low to high surface tension (Marangoni, 1865). When the upper surface is a rigid lid, as holds for many experiments performed, no Marangoni effects occur. *See example Ex. 1.3*

For experiments in rectangular containers, with length L, width B, and height D, the flow is characterized by the two aspect ratios $A_x = L/D$ and $A_y = B/D$, and four other parameters, namely the Rayleigh number Ra, the Prandtl number Pr, the Marangoni number Ma, and the Biot number Bi, defined by

$$Ra = \frac{\alpha_T g \Delta T D^3}{\nu\kappa}; \ Pr = \frac{\nu}{\kappa} \ ; \ Ma = \frac{\sigma_0 \gamma_T \Delta T D}{\rho_0 \nu\kappa} \ ; \ Bi = \frac{hD}{k},$$

where h is a (constant) surface heat transfer coefficient, $\nu = \mu/\rho_0$ is the kinematic viscosity, and $\kappa = k/(\rho_0 C_p)$ the thermal diffusivity.

For pure Rayleigh–Bénard convection, when the upper surface is a rigid wall, the parameters Bi and Ma do not appear; an experimentally determined regime diagram in the $Pr - Ra$ space is shown in Fig. 1.5a. The critical value of Ra in this case (with rigid bottom wall and A_x, $A_y \to \infty$) is $Ra_c = 1707.8$. In this case, roll cells appear above criticality; a sketch of such a flow pattern is shown in Fig. 1.5b. The Ra range
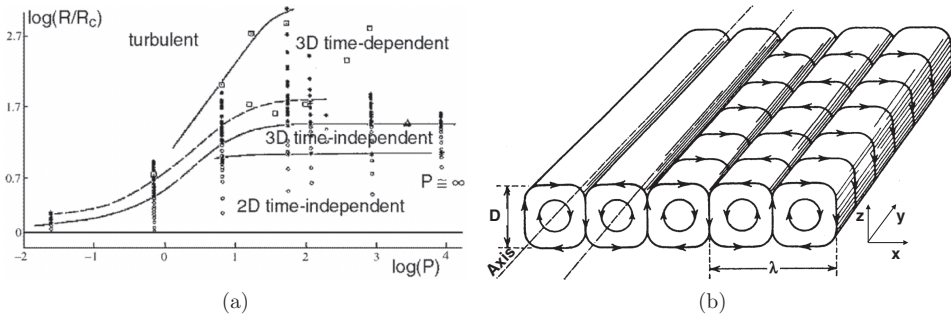
Figure 1.5 (a) Regime diagram in the *Pr* − *Ra* space for pure Rayleigh–Bénard convection (Krishnamurti, 1973), where *P* = *Pr* and *R* = *Ra*. (Published with permission from Cambridge University Press.) (b) Sketch of a pattern of roll cells in a rectangular container.

of steady roll cells is much larger for larger *Pr* liquids and disappears from liquids like mercury having a very small *Pr*. When *Ra* is increased, time dependence also occurs and finally the flow becomes turbulent.

For pure Bénard–Marangoni convection, we have $Ra = 0$ and the critical Marangoni number Ma_c depends on *Bi*; for $Bi = 0$ and again $A_x, A_y \to \infty$, its value is 79.6. There is no experimentally determined regime diagram of pure Bénard–Marangoni flows, since buoyancy effects are difficult to eliminate. It could, in principle, be done in space, but is practically difficult to carry out.

1.4.2 Governing Equations

In deriving the governing equations from the general equations in Section 1.1, often the Boussinesq approximation is made, which (in short) assumes that density variations are so small compared to the reference density ρ_0 that they only have to be taken into account in the volume (in this case buoyancy) force. The equations then become

$$\frac{\partial u}{\partial t} + u\frac{\partial u}{\partial x} + v\frac{\partial u}{\partial y} + w\frac{\partial u}{\partial z} = -\frac{1}{\rho_0}\frac{\partial p}{\partial x} + \nu\nabla^2 u + f_x, \qquad (1.13a)$$

$$\frac{\partial v}{\partial t} + u\frac{\partial v}{\partial x} + v\frac{\partial v}{\partial y} + w\frac{\partial v}{\partial z} = -\frac{1}{\rho_0}\frac{\partial p}{\partial y} + \nu\nabla^2 v + f_y, \qquad (1.13b)$$

$$\frac{\partial w}{\partial t} + u\frac{\partial w}{\partial x} + v\frac{\partial w}{\partial y} + w\frac{\partial w}{\partial z} = -\frac{1}{\rho_0}\frac{\partial p}{\partial z} + \nu\nabla^2 w + f_z, \qquad (1.13c)$$

$$\frac{\partial u}{\partial x} + \frac{\partial v}{\partial y} + \frac{\partial w}{\partial z} = 0, \qquad (1.13d)$$

$$\frac{\partial T}{\partial t} + u\frac{\partial T}{\partial x} + v\frac{\partial T}{\partial y} + w\frac{\partial T}{\partial z} = \kappa\nabla^2 T, \qquad (1.13e)$$

with $f_x = f_y = 0$ and $f_z = -\rho g/\rho_0 = -g(1 - \alpha_T(T - T_0))$. In these equations, (x, y, z) are the Cartesian coordinates of a point in the liquid layer, t denotes time, (u, v, w) is the velocity vector, p denotes pressure, and T is the temperature.

The lower boundary of the liquid (Fig. 1.4a) is considered to be a very good conducting boundary on which the temperature is constant T_B, and no-slip conditions apply. On the lateral walls (at $x = 0, L$ and $y = 0, B$), no-flux and no-slip conditions are prescribed. Let the non-deforming gas–liquid interface be located at $z = D$; then the general boundary conditions become

$$x = 0, L: \qquad\qquad u = v = w = \frac{\partial T}{\partial x} = 0, \qquad\qquad (1.14a)$$

$$y = 0, B: \qquad\qquad u = v = w = \frac{\partial T}{\partial y} = 0, \qquad\qquad (1.14b)$$

$$z = 0: \qquad\qquad T = T_B \ ; \ u = v = w = 0, \qquad\qquad (1.14c)$$

$$z = D: \quad \mu\frac{\partial u}{\partial z} = \frac{\partial \sigma}{\partial x} \ ; \ \mu\frac{\partial v}{\partial z} = \frac{\partial \sigma}{\partial y} \ ; \ w = 0 \ ; \ k\frac{\partial T}{\partial z} = h(T_A - T), \ (1.14d)$$

where T_A is the temperature of the gas just above the interface. The first two equations in (1.14d) represent the Marangoni effect, and the last equation is the surface heat transfer condition. *See example Ex. 1.4*

For $\bar{u} = \bar{v} = \bar{w} = 0$, there is a steady state given by

$$\bar{T}(z) = T_B - \beta z; \ \beta = \frac{h(T_B - T_A)}{k + hD}, \qquad\qquad (1.15)$$

where β is the vertical temperature gradient over the layer. The corresponding pressure distribution is readily determined from (1.13), and if one chooses $T_0 = T_A$, this gives

$$\bar{p}(z) = p_0 + \rho_0 g \left((\alpha_T(T_B - T_A) - 1)z - \frac{\alpha_T \beta}{2}z^2 \right). \qquad\qquad (1.16)$$

This motionless solution is characterized by only conductive heat transfer and is easily realized in laboratory experiments. Note that such a motionless solution exists for all values of the vertical temperature difference, $\Delta T = \beta D$.

If the upper surface is a rigid surface and kept at a constant temperature T_A, there are no Marangoni effects and the surface temperature is kept constant ($h \to \infty$ in (1.14)). In this case of pure Rayleigh–Bénard convection, the boundary conditions (1.14d) are replaced by

$$z = D: u = v = w = 0, T = T_A. \qquad\qquad (1.17)$$

The analytic solution for temperature (1.15) in this case still holds, but the limit $h \to \infty$ has to be taken for which $\beta \to (T_B - T_A)/D$.

> **Additional Material**
>
> - An extensive overview of experimental work on the Rayleigh–Bénard–Marangoni flows is given in Koschmieder (1993) and Getling (1998).
> - The Bénard Centenary Review (Mutabazi *et al.*, 2010) contains many very interesting papers on Bénard's experiments and their extensions; also included is a great scientific biography of Henri Bénard by José Eduardo Wesfreid (pages 9–37).

1.5 Differentially Heated Cavity Flow

Because of its engineering importance, the flow in a cavity of which two opposite vertical sidewalls have different temperatures has been studied extensively. The main aim of these studies was to determine the heat transport from the heated wall towards the cooler wall.

1.5.1 Experimental Results

The first experiments with air in containers of different aspect ratios were performed by Eckert and Carlson (1961). As in the Rayleigh–Bénard problem, the flow is characterized by two aspect ratios $A_x = L/D$ and $A_y = B/D$, the Rayleigh number Ra, and the Prandtl number Pr. Eckert and Carlson (1961) used the Grashof number $Gr = Ra/Pr$ and showed that the flow is stationary up to a critical value (Gr_c) and unsteady thereafter.

Elder (1965) performed experiments in a container with $A_y >> A_x$ (such that the flow is approximately two-dimensional) while varying D/L over the range $[1, 60]$ for a liquid with $Pr = 10^3$. A sketch of the experimental configuration is shown in Fig. 1.6a. The value of Ra in Elder (1965) is based on the length L and given by

$$Ra = \frac{\alpha_T g \Delta T L^3}{\nu \kappa}. \tag{1.18}$$

For small values of Ra there is a wall-to-wall flow, the liquid descending along the cold wall and moving upward along the warm wall. Flow profiles for different values of Ra (Fig. 1.6b) show that secondary flows develop for higher Ra. The wavelength of these flows decreases with increasing values of Ra.

In an extensive series of experiments, Jannot and Mazeas (1973) determined (for the same configuration as in Elder (1965)) the Ra boundary between stationary and non-stationary regimes, namely the onset of time dependence in the flow. However, there does not appear to be a full experimental regime diagram of this flow. Variations of the configuration were introduced by Hart (1971), including
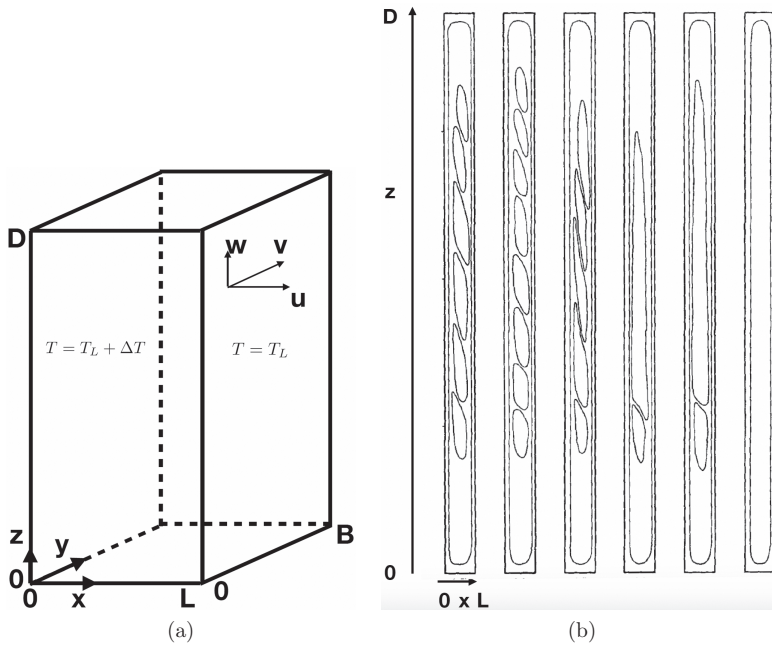
Figure 1.6 (a) Sketch of the experimental set-up used in Elder (1965). (b) Sketch of flows visualized (Elder, 1965) for different values of *Ra* (for *L* = 2 cm and *D* = 38 cm) with *Ra* increasing from right to left, showing the appearance of secondary flows with larger *Ra*. (Published with permission from Cambridge University Press.)

the effects of angular rotation (for their geophysical relevance), and by Imberger (1974), studying flows for very large A_x.

1.5.2 Governing Equations

The equations describing the Differentially Heated Cavity flow are the same as for the pure Rayleigh–Bénard problem (1.13) and are not repeated here; also, a linear equation of state is assumed to be adequate. The vertical sidewalls at $x = 0$ and $x = L$, which have a different temperature, are considered to be extremely good conducting boundaries on which the temperature is constant, and no-slip conditions apply. On the other walls (at $z = 0, D$ and $y = 0, B$) no-flux and no-slip conditions are prescribed. The boundary conditions then become (Fig. 1.6a) *See example Ex. 1.5*

$$x = 0: \quad u = v = w = T - (T_L + \Delta T) = 0, \tag{1.19a}$$

$$x = L: \quad u = v = w = T - T_L = 0, \tag{1.19b}$$

$$y = 0, B: \quad u = v = w = \frac{\partial T}{\partial y} = 0, \tag{1.19c}$$

$$z = 0, D: \quad u = v = w = \frac{\partial T}{\partial z} = 0. \tag{1.19d}$$

There is no elementary analytical solution for the differentially heated cavity problem, as even small temperature differences ΔT will cause a non-trivial flow in the cavity.

Additional Material

- An extensive, although already a bit dated, review on experimental work regarding the Differentially Heated Cavity flow can be found in Paolucci (1994). Variants of this flow, which also show very interesting behaviour, are laterally heated/cooled containers which are inclined with respect to gravity (Saury *et al.*, 2012).

1.6 Summary

- Fluid flows can undergo staged transitions when parameters, for example those related to the forcing of the flow, are varied. For large forcing (with respect to viscous and diffusive processes), turbulent flows result.
- We have focused on four classical flows: the Lid-Driven Cavity flow, the Taylor–Couette flow, the Rayleigh–Bénard–Marangoni flow, and the Differentially Heated Cavity flow. These flows have been studied extensively in laboratory experiments.
- For the Taylor–Couette flow and the Rayleigh–Bénard–Marangoni flow analytical parallel flow solutions exist. These become unstable at specific values of Reynolds and Rayleigh/Marangoni numbers, respectively, and non-parallel patterned flows (Taylor vortices and hexagonal/roll cell patterns) result.
- For even higher values of these parameters, a transition to time dependence occurs, resulting, for example, in wavy Taylor vortices in the Taylor–Couette flow.
- For the Lid-Driven Cavity flow and the Differentially Heated Cavity flow, no such parallel steady flow solutions exists, but the non-parallel steady flows also become unstable at specific values of the Reynolds and Rayleigh numbers, respectively.
- For each of the classical flows, the fluid dynamical equations and boundary conditions describe the dominant balances of mass, momentum, and heat in unprecedented detail.

1.7 Exercises

Exercise 1.1 *Consider the two-dimensional Lid-Driven Cavity flow in Cartesian coordinates (x, z) in a container of length L and height D. In this case, the stream function ψ can be introduced through*

$$u = \frac{\partial \psi}{\partial z} \; ; \; w = -\frac{\partial \psi}{\partial x}$$

We can, furthermore, non-dimensionalize the equations through scales L for length, U for velocity, and L/U for time.

a. Show that the governing equations can be written as

$$\frac{\partial \zeta}{\partial t} + \boldsymbol{u} \cdot \nabla \zeta = Re^{-1} \nabla^2 \zeta$$

$$\zeta = -\nabla^2 \psi,$$

where $\zeta = \partial w/\partial x - \partial u/\partial z$ is the vertical component of the vorticity vector and $Re = UL/\nu$.

b. Formulate the boundary conditions for ψ.

Exercise 1.2 *Consider the Taylor–Couette flow in the case $\omega_i = \omega$ and $\omega_o = 0$. A steady solution can be found of the form $\bar{u} = \bar{w} = 0$ and $\bar{v} = \bar{v}(r, z)$.*

a. Show that the governing equations for $\bar{v}$ become

$$\frac{1}{r} \frac{\partial}{\partial r} \left(r \frac{\partial \bar{v}}{\partial r} \right) + \frac{\partial^2 \bar{v}}{\partial z^2} - \frac{\bar{v}}{r^2} = 0$$

with boundary conditions $r = r_i$: $\bar{v} = \omega r_i$; $r = r_o$: $\bar{v} = 0$; and $z = 0, L$: $\bar{v} = 0$.

b. Argue that when the vertical direction is unbounded, $L \to \infty$, that $\bar{v} = \bar{v}(r)$.

c. Determine $\bar{v}(r)$ and $\bar{p}(r, z)$ and compare with (1.10).

Exercise 1.3 *Consider a fluid particle in a motionless liquid under a vertical temperature gradient in the Rayleigh–Bénard–Marangoni experiment. Assume that the particle is moved upwards adiabatically.*

First, consider the case that the surface tension is constant and the particle is far from the air–liquid surface.

a. Sketch and determine the forces on the particle just after the perturbation.

b. Argue that the perturbation motion is amplified if some critical value of the Rayleigh number Ra is exceeded.

Next, consider the case that gravity is absent, but surface tension is a monotonically decreasing function of temperature and the particle is moved to the surface.

c. Sketch and determine the forces on the particle just after the perturbation.

d. Argue that the perturbation motion is amplified if some critical value of the Marangoni Ma is exceeded.

Exercise 1.4 *Consider the pure Rayleigh–Bénard problem as in Section 1.4.2 and the case of an upper rigid surface with a fixed temperature T_A.*

a. When $Ra < Ra_c$, the liquid is motionless. Determine the equations for the temperature field and the pressure field.

b. Argue that the temperature $\bar{T}$ and pressure $\bar{p}$ are only functions of z.

c. Use the boundary conditions to determine the basic state solution $(\bar{T}, \bar{p})$ and compare to the solution given in Section 1.4.2.

Exercise 1.5 *Consider the two-dimensional Differentially Heated Cavity flow in a Cartesian coordinate system (x, z). Make the equations non-dimensionless, by using scales $g\alpha_T \Delta T D^3/(\nu L)$ for velocity, D for length, and $\nu L/(g\alpha_T D^2 \Delta T)$ for time, and define a dimensionless temperature ϑ by $\vartheta = (T - T_L)/\Delta T$. Furthermore, introduce a stream function ψ such that*

$$u = \frac{\partial \psi}{\partial z} \; ; \; w = -\frac{\partial \psi}{\partial x}.$$

a. Show that the dimensionless equations are given by

$$GrA^2 \left(\frac{\partial \zeta}{\partial t} + u\frac{\partial \zeta}{\partial x} + w\frac{\partial \zeta}{\partial z} \right) = A\nabla^2\zeta + \frac{\partial \theta}{\partial x},$$

$$\nabla^2\psi = -\zeta,$$

$$GrPrA \left(\frac{\partial \vartheta}{\partial t} + u\frac{\partial \vartheta}{\partial x} + w\frac{\partial \vartheta}{\partial z} \right) = \nabla^2\vartheta,$$

where ζ is the vertical component of the vorticity vector. The boundary conditions are

$$x = 0: \qquad \psi = \frac{\partial \psi}{\partial x} = \vartheta = 0,$$

$$x = 1/A: \quad \psi = \frac{\partial \psi}{\partial x} = \vartheta - 1 = 0,$$

$$z = 0, 1: \qquad \psi = \frac{\partial \psi}{\partial z} = \frac{\partial \vartheta}{\partial z} = 0,$$

where $A = 1/A_x = D/L$ and $Pr = \nu/\kappa$. Give an expression for the Grashof number Gr in this case.

Next, we try to find asymptotic solutions in the limit $A \to 0$ of the form

$$\vartheta = \vartheta_0 + A\vartheta_1 + A^2\vartheta_2 \cdots ; \quad \psi = \psi_0 + A\psi_1 + A^2\psi_2 \cdots$$

b. Show that

$$\psi \sim K_1 \left(\frac{z^4}{24} - \frac{z^3}{12} + \frac{z^2}{24} \right),$$

$$\vartheta \sim K_1 x + K_2 + K_1^2 GrPrA^2 \left(\frac{z^5}{120} - \frac{z^4}{48} + \frac{z^3}{72} \right)$$

with constants K_1 and K_2.

c. Describe a procedure for how the constants K_1 and K_2 can be determined.